J. Fluid Mech. (2010), *vol.* 658, *pp.* 310–335.
doi:10.1017/S0022112010001758

Quadrant analysis of a transitional boundary layer subject to free-stream turbulence

K. P. NOLAN[1]†, E. J. WALSH[1] AND D. M. McELIGOT[2,3]

[1]Stokes Institute, Department of Mechanical and Aeronautical Engineering, University of Limerick, Ireland

[2]Idaho National Laboratory (INL), Idaho Falls, ID 83415-3885, USA

[3]University of Arizona, Department of Aerospace and Mechanical Engineering, AZ 85721, USA

(Received 22 July 2009; revised 5 April 2010; accepted 8 April 2010;
first published online 30 June 2010)

This paper presents analyses of particle image velocimetry measurements from a boundary layer on a flat plate subject to grid-generated free-stream turbulence. The pre-transition region and early stages of breakdown to turbulent spots are explored by means of quadrant analysis and quadrant hole analysis. By isolating the contributors to the Reynolds shear stresses, it is possible to identify coherent structures within the flow that are responsible for the production of TKE. It is found that so called 'ejection' events are the most significant form of disturbance, exhibiting the largest amplitude behaviour with increased negative spanwise vorticity. Sweep events become increasingly large close to the wall with increased Reynolds number and intermittency.

Key words: boundary-layer transition, instability, streaks, turbulent spots

1. Introduction

The breakdown to turbulence in wall-bounded flows is a fundamental problem in fluid mechanics. Natural transition, where Tollmein–Schlichting (TS) waves become unstable and form Λ structures which then breakdown into turbulent spots, is often bypassed by transition induced by free-stream disturbances where the root mean square of the free-stream disturbances at the leading edge exceeds about 1 % of the mean free stream. Klebanoff (1971) was the among the first to identify longitudinal streaks resulting from free-stream buffeting. These appear as long narrow streamwise structures, which maintain a relatively constant velocity surplus or deficit relative to the local convection velocity, and are consequently referred to as positive and negative streaks respectively. Numerous researchers have since investigated this streaky behaviour and elucidated their role in several breakdown scenarios. Rapid distortion theory, reviewed by Durbin & Wu (2007), explains the formation of a longitudinal streak from a large-scale free-stream disturbance when it enters a shearing flow. The transition process becomes dominated by the influences of these streaks which, in turn, accelerates the breakdown to turbulence. Counter intuitively Fransson *et al.* (2006) showed experimentally how negative streaks induced with cylindrical roughness elements can have a stabilizing effect on transition in a low free-stream turbulence environment by damping TS waves. Similarly, the large-eddy simulation of

† Email address for correspondence: kevin.nolan@ul.ie

Schlatter, Brandt & De Lange (2007) showed that the onset of classical transition can be delayed by a critical level of free-stream turbulence and therefore concentration of streaks.

Several streak breakdown scenarios have been elucidated from direct numerical simulations (DNS). Jacobs & Durbin (2001) and Zaki & Durbin (2005) have identified a source of breakdown due to the lift up of negative streaks towards the boundary-layer edge. This phenomenon acts as a receptivity path for high-frequency free-stream disturbances otherwise dissipated by the shear filtering process. Meanwhile Brandt, Schlatter & Henningson (2004) and Brandt & de Lange (2008) have shown that instabilities within the streaks are sufficient to initiate a breakdown. The former scenario shows that breakdown is initiated near the boundary-layer edge, resulting in Jacobs & Durbin (2001) making the distinction between 'top-down' and 'bottom-up' spots in a reference to the techniques often used to generate artificial turbulent spots by many experimentalists in the literature (Cantwell, Coles & Dimotakis 1978; Sabatino, Smith & Smith 2002; Chong & Zhong 2005; Yaras 2007). The simulations of Zaki & Durbin (2005) have expanded this scenario by showing that bypass transition will occur when both a penetrating and a non-penetrating Orr–Somerfeld mode are applied to the model inlet. Bypass transition was found only to occur with the presence of both a penetrating mode and a non-penetrating mode. The latter scenario of Brandt *et al.* (2004) shows that the shear interface that forms between upstream positive streaks and downstream negative streaks as they collide is itself sufficient to generate an instability close to the wall.

Consequently, it is found that the influence of streaky structures on the laminar boundary layer is far from simple. Streaks may either delay or promote transition to turbulence depending on their spatial arrangement within the boundary layer. How these special conditions translate into the real-world applications is currently unknown. The detailed hot-film measurements of Anthony, Jones & LaGraff (2005) perhaps provide some of the most insightful experimental data on the bypass transition scenario. Their measurements indicate that, in the presence of free-stream turbulence, streak-like structures with elevated unsteady heat flux characteristics occasionally precede the breakdown to turbulence at the wall. The nature of the measurement technique used prevented similar measurements away from the wall in this study to further identify regions of breakdown.

This paper presents a detailed examination of the contributions to the Reynolds shear stress, and hence the production of turbulent kinetic energy (TKE), within the pre-transitional and transitional boundary layer in the streamwise wall-normal (X–Y) plane. Comparisons with the findings of the DNS studies discussed above will drawn in order to shed further light on the transition process. Instantaneous high-speed particle image velocimetry (PIV) data are decomposed into quadrants after the method proposed by Willmarth & Lu (1972), and further into regions of significant contributions to the Reynolds shear stress identified and investigated using the quadrant hole method after Lu & Willmarth (1973). It is observed that the production of TKE peaks away from the wall in the pre-transitional region, although well within the boundary layer, moving steadily towards the wall with the formation of turbulent spots. Ejection events (corresponding to negative u', positive v') resulting from lifted slow-moving streaks are found to dominate the outer region of the boundary layer with associated elevated vorticity and amplitude as the Reynolds number increases. Meanwhile sweep events (corresponding to positive u', negative v') grow increasingly significantly close to the wall. Finally, a power-law approximation of the relationship between the Reynolds shear stress contribution of the four quadrants

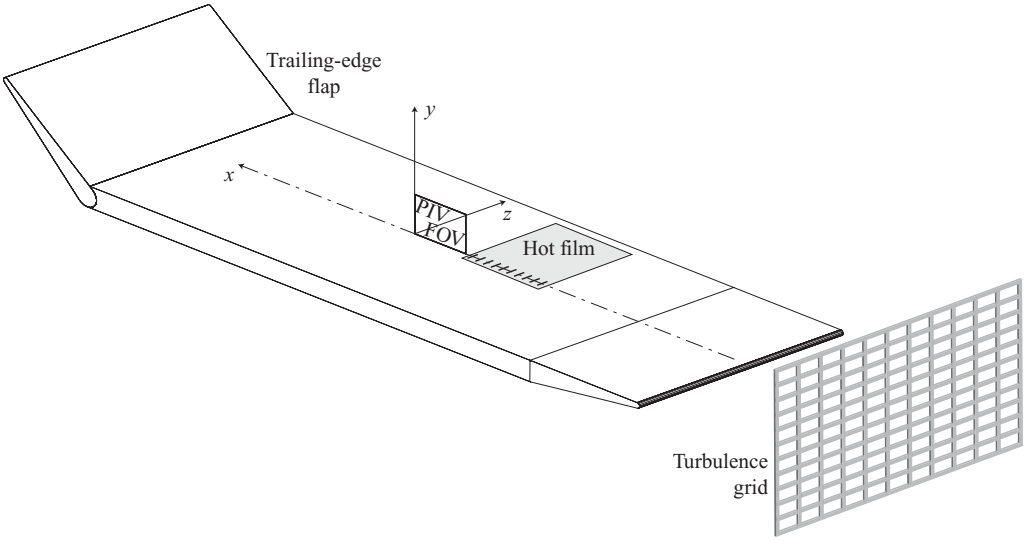

FIGURE 1. Sketch of flat-plate model with turbulence grid illustrating the location of the hot-film array and PIV field of view (FOV).

and the percentage of time resulting in this contribution is introduced and is of use to the turbulence modelling community.

2. Experimental set-up and procedure

Experiments were performed in a non-return medium-speed wind tunnel. This facility is described in detail by Hernon, Walsh & McEligot (2007). The test section is 1 m in length and has a 300 mm $\times$ 300 mm cross-section. Velocities up to 100 m s^{-1} can be reached in the test section with a background turbulence intensity of 0.2 %. Figure 1 shows an illustration of the flat-plate model used for measurements.

The plate is constructed in a modular configuration, from three sections of 10 mm aluminum plate, is 1 m in total length, 0.3 m in span and has a 2 mm diameter semicylindrical leading-edge section which chamfers asymmetrically to the plates underside over a length of 90 mm while preserving the flat upper surface. The plate also incorporates a trailing-edge flap, a configuration used extensively in the literature, which is used to control the position of the leading-edge stagnation point and hence any separation may occur at the leading edge. Liquid shear crystal measurements and china clay visualization by Walsh *et al.* (2005) of the effect of the flap on the leading edge have shown that a positive flap angle of 45° provides an attached flow resulting in the growth of a laminar boundary layer which gives excellent agreement with the Blasius solution for a laminar boundary layer under low levels of free stream turbulence (FST).

A turbulence grid, placed at least 10 mesh lengths upstream of the leading edge, is used to generate sufficiently homogeneous isotropic free-stream turbulence. Hernon *et al.* (2007) described the construction of a range of turbulence generating grids available. Designed to the criteria devised by Roach (1987), the grids are placed at the inlet to the test section sandwiched between the inlet contraction and the test section. A single turbulence grid was used throughout the current PIV study as it provided the best overall suitability for spatial and temporal resolution in terms of flow properties such as boundary layer thickness, free-stream velocity and the limitations of optical

Parameter	
Grid bar width (mm)	2.6
Mesh length (mm)	25.2
% Grid solidity	20
% Tu_{max}	4.3
% Tu_{min}	2
% $Tu_{current}$	4.3
$\Lambda_{x(max)}$ (mm)	15
$\Lambda_{x(min)}$ (mm)	5
$\Lambda_{x\,current}$ (mm)	6.7

TABLE 1. Range of turbulence grid properties for the grid used at the plate leading edge and conditions for the current study from Hernon *et al.* (2007).

access to the tunnel test section. The range of free-stream turbulence characteristics available, by varying the distance between the plate leading edge and grid, as well as those used in the current study are summarized in table 1.

A commercial PIV system, supplied by TSI Inc., was used for measurements. The system is comprised of a 50 mJ Litron nano L laser, Synchronizer Model 610035, HS200 high-speed camera (640 pixel $\times$ 480 pixel resolution) with a Nikkor 50 mm f1.8 lens giving a field of view 25 mm $\times$ 35 mm at an acquisition frame rate of 90 Hz. Seeding was provided by using a commercial fog machine which evaporates glycol oil. The boundary layer was sufficiently seeded by flooding the laboratory with seeding smoke for a period of time prior to measurements. Velocity vectors were processed using an iterative second-order recursive deformation processing technique available in the INSIGHT 3G software package. This algorithm has an experimental uncertainty of 0.3 % which was measured using synthetic particle images. This results in a total uncertainty of 0.7 % in the PIV measurements when including the uncertainty of the synchronizer and spatial calibration. An AA Labs AN-1005 hot-wire anemometry system was used with a surface mounted hot-film array. The main advantage of the AN-1005 is that it uses a powerful optically isolated data acquisition system that is capable of sampling all four channels at 16 bit resolution at sampling rates of up to 500 kHz. The data are acquired directly by a bi-directional parallel port. There is a range of low-pass filter settings on the AN-1005 from 1 Hz to 14 kHz. The hot-film array is a Senflex 9101 consisting of 50 elements with 2.54 mm element spacing. The array is placed on the surface with an acrylic pressure sensitive adhesive (MACfilm IF-2043).

The Reynolds number was varied by maintaining streamwise position and varying the free-stream velocity. A consequence of this approach is that the ratio of free-stream turbulent length scales to boundary-layer thickness will vary for each case. Table 2 details the flow properties recorded for the eight cases considered. Cases A–D correspond to pre-transitional cases while the remaining cases are located within the transition region. Measurements were performed in the X–Y (streamwise–wall normal) plane for all the cases considered.

Each case consists of 10 s of concurrent hot-film and PIV sampling. The PIV image pairs were sampled at 90 Hz while hot-film measurements were sampled at 10 kHz and cut off at 3.8 kHz in accordance with the Nyquist theorem. The turbulence intensity (% Tu) at the leading edge of the flat plate for the configuration used was 4.3 % as measured by Hernon *et al.* (2007). The PIV field of view begins at 0.4 m

Case	U_∞(m s^{-1})	$Re_x \times 10^3$	Re_θ	δ(mm)	H_{12}	$\%Tu(x)_\infty$	γ	Y^+_{min}
A	0.79	21.2	111	15.89	2.45	3.34	0	3.5
B	1.33	35.6	142	13.16	2.48	2.95	0	5.6
C	1.71	45.9	151	11.79	2.55	3.19	0	7.0
D	2.32	62.3	178	10.88	2.48	2.88	0.049	8.8
E	2.74	73.6	186	10.43	2.25	2.96	0.110	10.4
F	3.41	91.5	240	10.88	1.78	2.73	0.252	13.0
G	3.66	98.3	264	10.88	1.64	3.48	0.304	14.6
H	4.39	117.9	314	11.34	1.51	3.15	0.531	17.4

TABLE 2. Flow properties for all measurement cases detailing free-stream velocity, Reynolds number, boundary-layer thickness, shape factor, local free-stream turbulence intensity, hot-film intermittency level and resolved PIV proximity to the wall.

from the plate leading edge just upstream of and in line with the final sensor of the hot-film array which is located at 0.38 m (figure 1).

2.1. *Quadrant mapping*

Traditionally, measurements of turbulent fluid flow are decomposed according to the Reynolds decomposition, $u = \overline{U} + u'$, etc. In an attempt to further extricate the structure of turbulent events Willmarth & Lu (1972) separated the Reynolds shear stresses into quadrants (Q1–Q4) as shown in figure 2. The fluctuating components of velocity are conditionally sampled into respective quadrants. Ejection events, $-u' + v'$, and sweep events, $+u' - v'$, are found to be the main contributor to the transfer of vertical momentum within the turbulent boundary layer (Alfredsson & Johansson 1984). Such decomposition has also been used to characterize structures within artificial spots (Schrder & Kompenhans 2004) and hairpin vortices (Adrian, Meinhart & Tomkins 2000) where structures are described by the spatial arrangement of different quadrants.

Once the data have been segregated into the four quadrants, the average shear stress associated with each quadrant can be determined from

$$\overline{u'v'_i} = \frac{1}{N}\sum_{n=1}^{N}\left[u'v'_i(t)\right]_n, \quad i = 1\ldots4, \tag{2.1}$$

where

$$\sum_{i=1}^{4}\overline{u'v'_i} = \overline{u'v'}. \tag{2.2}$$

Here N is the number of samples, n is the current sample number and i is the quadrant number.

2.2. *Quadrant hole analysis*

Quadrant hole analysis is used to measure the extent of contributions to the Reynolds shear stress in each quadrant by further limiting the data to consider values above a certain-amplitude threshold. Figure 3 shows a scatter plot of the two fluctuating components of velocity (u' and v') for a single wall-normal location in a typical data set. By thresholding the data with $|u'v'| = $ const. regions greater than this reference constant shear stress (solid curved lines in figure 3) may be isolated. The threshold

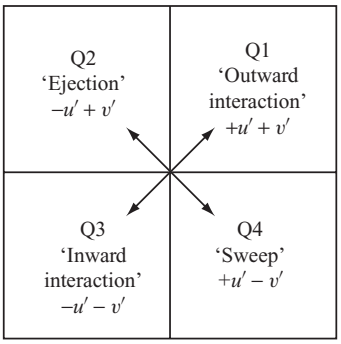

FIGURE 2. Quadrant decomposition of the fluctuating components of velocity for a flow from left to right.

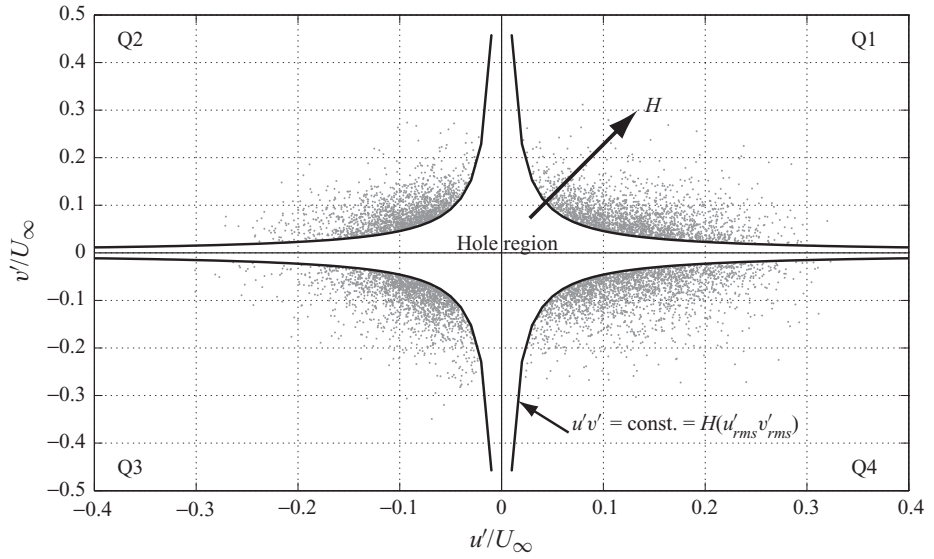

FIGURE 3. Illustration of the quadrant hole analysis technique for a typical data set illustrating the threshold level at a single value of H (defined in (2.3)) for each quadrant. Data in the hole region have been removed for clarity.

level, TH, is determined from a multiple (H) of the root-mean-square (r.m.s.) stress:

$$TH = H\left(u'_{rms}v'_{rms}\right). \tag{2.3}$$

This threshold, when applied to each quadrant, defines the 'hole region' in figure 3 where the data have been removed. By increasing the value of H, the hole region is enlarged and the fractional contribution of the remaining data, outside the hole, to the total shear stress can be determined. Zhu, van Hout & Katz (2007) define the duration fraction as the percentage time spent in a particular quadrant (i) that also satisfies the threshold level:

$$D^i_H = \frac{1}{N}\sum_{n=1}^{N} I^i_{H,n}, \tag{2.4}$$

where

$$I_H^i = \begin{cases} 1 & |uv(t)| > TH \text{ and the point } (u, v) \text{ is in qaudrant } i, \\ 0 & \text{otherwise,} \end{cases}$$

so that

$$\sum_{i=1}^{4} D_H^i(H) + D_H^h(H) = 1,$$

where h denotes the hole region. The quadrant's contribution to the total Reynolds shear stress can be determined in the form of a stress fraction after Lu & Willmarth (1973):

$$\frac{\widetilde{u'v'_i}(H)}{\overline{u'v'}} = \frac{1}{\overline{u'v'}} \frac{1}{N} \sum_{n=1}^{N} u'v'_i(t)\, I_H^i, \quad i = 1 \ldots 4, \tag{2.5}$$

so that

$$\sum_{i=1}^{4} \frac{\widetilde{u'v'_i}(H)}{\overline{u'v'}} + \frac{\widetilde{u'v'_h}(H)}{\overline{u'v'}} = 1. \tag{2.6}$$

Additionally, the mean vorticity associated with the data in each of the quadrants that satisfies the threshold can also be isolated:

$$\overline{\omega}_{zi} = \frac{\overline{\omega_z \left(I_H^i = 1\right)}}{\omega_z}, \; i = 1 \ldots 4. \tag{2.7}$$

The vorticity data may be further analysed by separating the instantaneous vorticity fields into positive and negative ω_z. By doing this it is possible to identify the main regions of positive and negative spanwise vorticity at various points within the flow. As noted by Zhu *et al.* (2007), (2.7) is not a fraction like (2.5) but rather a ratio of a subset of vorticity data to the time-averaged vorticity. Therefore the vorticity ratio in a given quadrant satisfying the threshold may increase with larger thresholds.

3. Results and discussion

Mean velocity profiles for the eight cases considered are shown in figure 4 in wall coordinates ($Y^+ = yu_\tau/\nu$, $U^+ = u/U$). Pre-transitional cases (A–D) are shown on the left and good agreement with the Blasius solution, shown in grey, is found when plotted in wall units. In the transition region (Cases E–H in figure 4*b*) the data deviates steadily from Blasius and shifts towards the von Kármán logarithmic law (Schlichting 1979) shown by a dashed line. Figure 5 shows hot-film time traces from Cases A, C , E and G. A number of turbulent spot signatures, identified by arrows, similar to those presented by Anthony *et al.* (2005) are found in Cases E and G.

Figures 6 and 7 show sequences of vector maps of the instantaneous perturbation field for Case C. Chronology is from top right to bottom left as this allows structures entering the field of view to be visualized as they might appear spatially. Only every fifth vector in the streamwise direction is shown to aid clarity. The contour level shows the streamwise perturbation while the horizontal dashed line represents the mean boundary-layer thickness at this location. A positive streak is visible in figure 6 and a negative streak in figure 7. The streaks are clearly identified by the dark streamwise perturbation contours. The negative streak exhibits a lift-up angle relative to the wall. In general, positive streaks are found to remain close to the wall while negative streaks generally approach and often surpass the mean boundary-layer

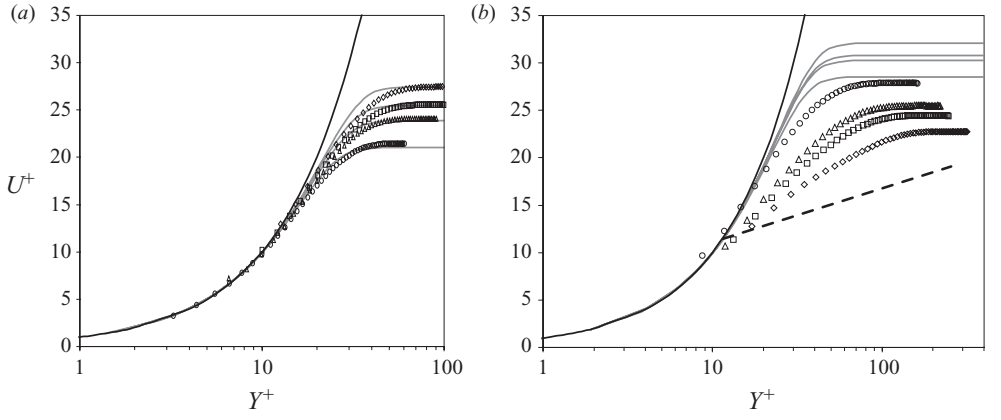

FIGURE 4. Mean velocity profiles: (*a*) pre-transitional Cases A–D, (*b*) transitional Cases E–H. Blasius solution shown by solid grey line. Cases A–D and E–H are shown by ○, △, □ and ◇, respectively for each plot.

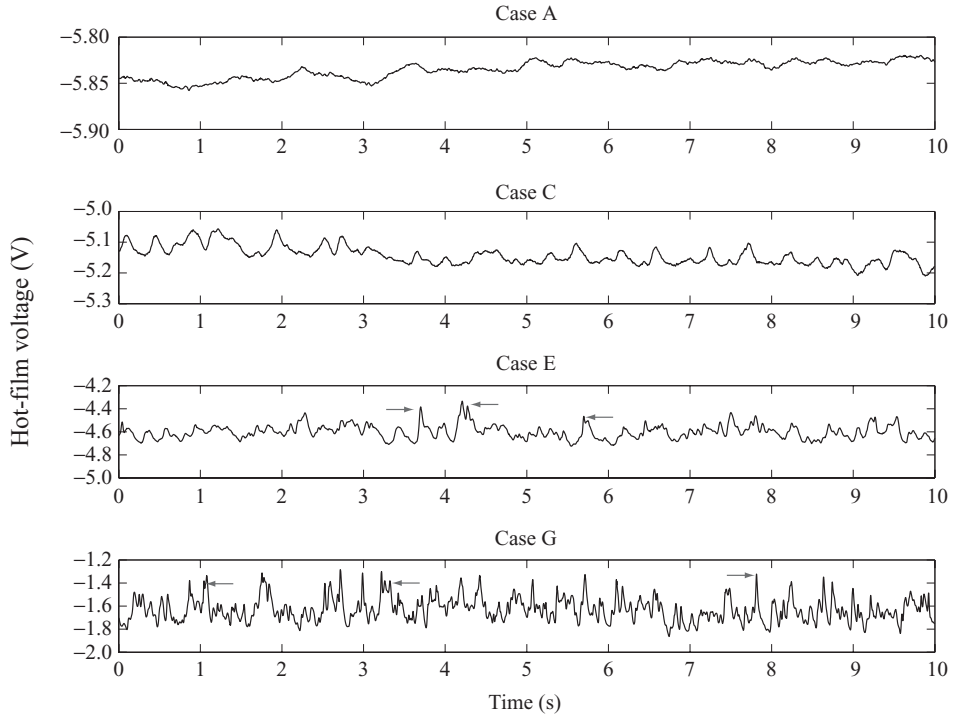

FIGURE 5. Hot-film time traces for pre-transitional Cases A and C, and transitional Cases E and G. Several turbulent spot signatures are noted with arrows.

thickness (shown as a dashed line) as also found by Hernon *et al.* (2007). As with the DNS findings of Jacobs & Durbin (2001) and Brandt *et al.* (2004), these streaks are primarily confined to the streamwise perturbation velocity rather than v' and w'.

Applying (2.1) to the data results in the plots shown in figure 8. These show the extent to which each quadrant contributes to the Reynolds shear stress in a time-averaged sense. For Case A the four quadrants are quite symmetrical peaking at

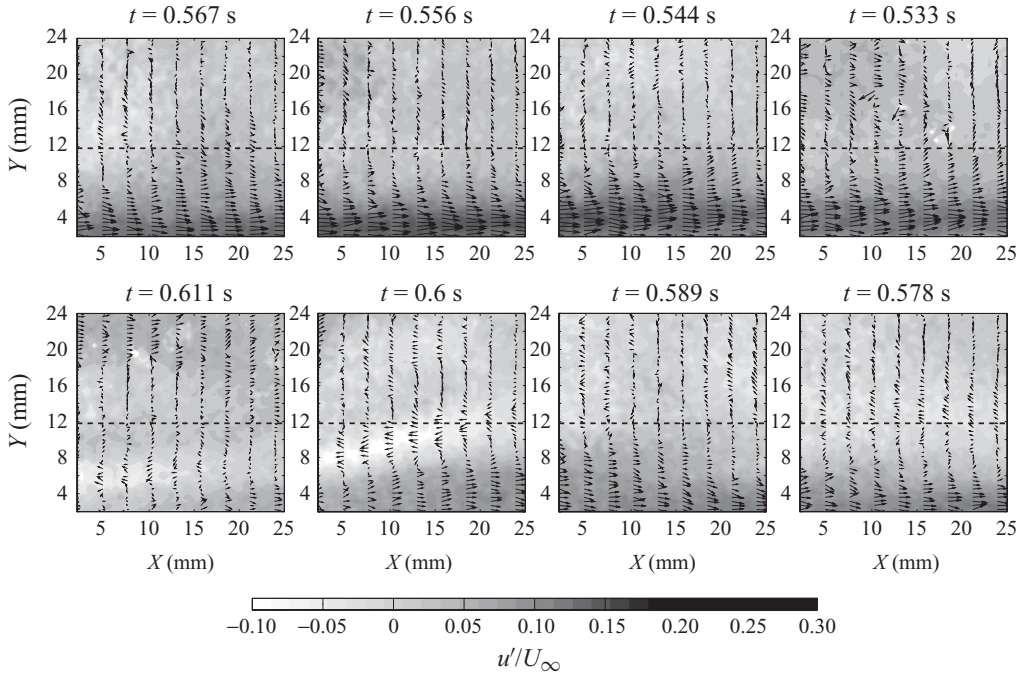

FIGURE 6. An example of a positive streak observed in Case C. Vectors show perturbation velocity while grey scale contours show streamwise perturbation. The dashed line indicates the position of the mean boundary-layer thickness.

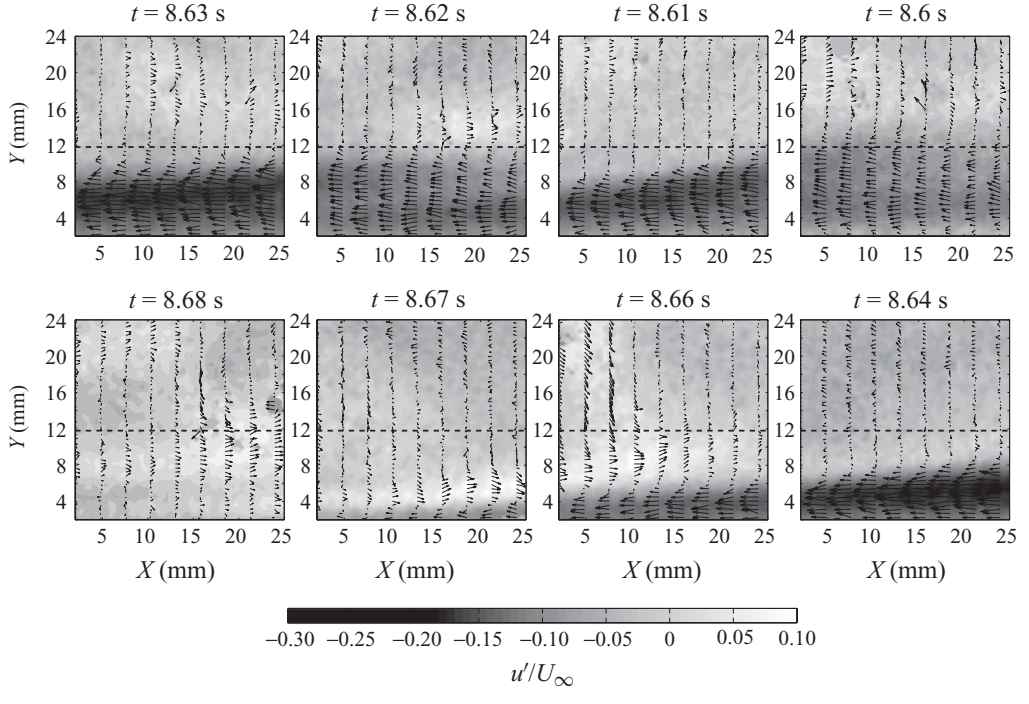

FIGURE 7. An example of a negative streak observed in Case C, as in figure 6.

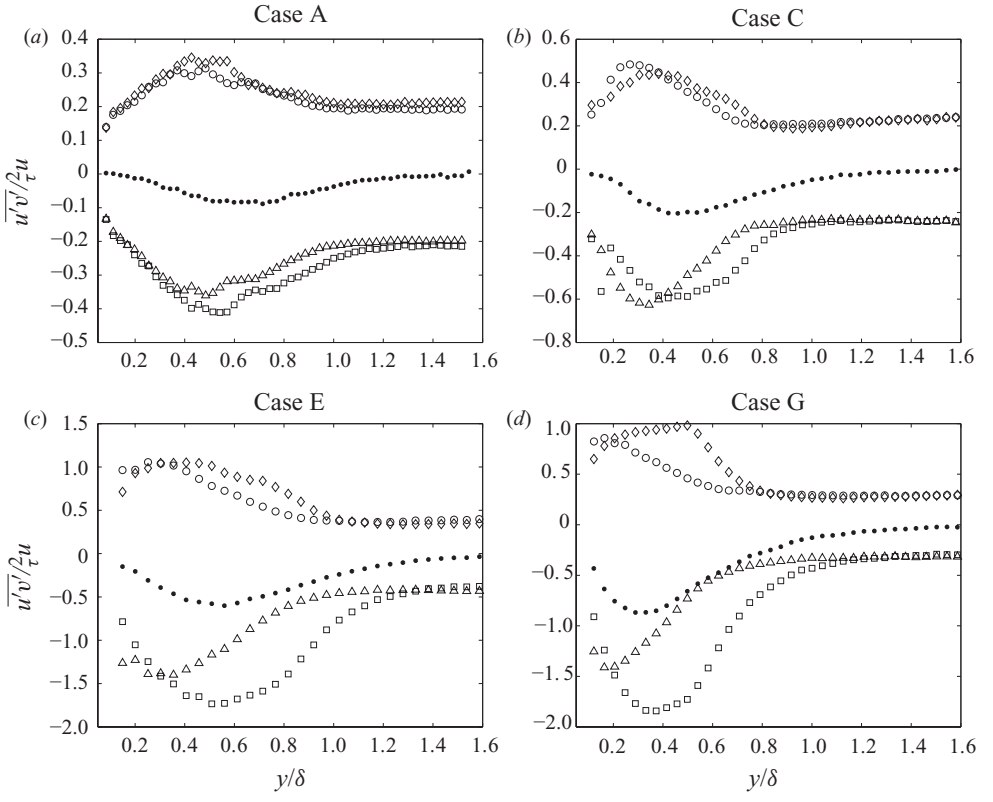

FIGURE 8. Reynolds shear stress for Cases A–G, and quadrant decomposed shear stress (defined in (2.1)), for Q1...4, ○, □, ◇ and △, respectively.

$y/\delta \approx 0.5$. Quadrant 2, denoted by open squares, has a small surplus compared to the others. By Case C the peaks in both quadrants 1 and 4, which correspond to positive u' fluctuations and hence those associated with positive streaks, have moved towards the wall at $y/\delta \approx 0.3$. The peak locations in the other quadrants remain unaffected. This trend continues for subsequent cases with the Q1 and Q4 peaks shifting to $y/\delta \approx 0.2$. Additionally, magnitude of the peak in ejection events, Q2, increases to almost double that of the positive quadrants, Q1 and Q3. Similarly, the peaks for sweeps, Q4, are 1.5 times greater than quadrants 1 and 3.

Figure 9 shows quadrant maps for the fluctuating component of velocity u' and v' for Cases A, C, E and G at various wall-normal distances. Rather than plot the data as a scatter plot, as in figure 3, the data have been contoured in terms of probability density and normalized by the local maximum at this wall-normal position. The plots in figure 9 are therefore joint probability density functions (PDFs) of the two fluctuating components of velocity u' and v'. The darkest regions of each joint PDF correspond to the greatest concentrations of instantaneous fluctuations for that position within the boundary layer. Looking at top plots in figure 9 at free-stream locations, $y/\delta > 0.99$, one sees the fluctuations appear evenly distributed and symmetrical. This observation indicates that the free-stream turbulence is nearly isotropic. The stretching of the streamwise fluctuations within the boundary layer is also clear in figure 9 at positions within the boundary layer. This is visible as the shape of the joint PDF changes from a circular shape to an elliptical shape,

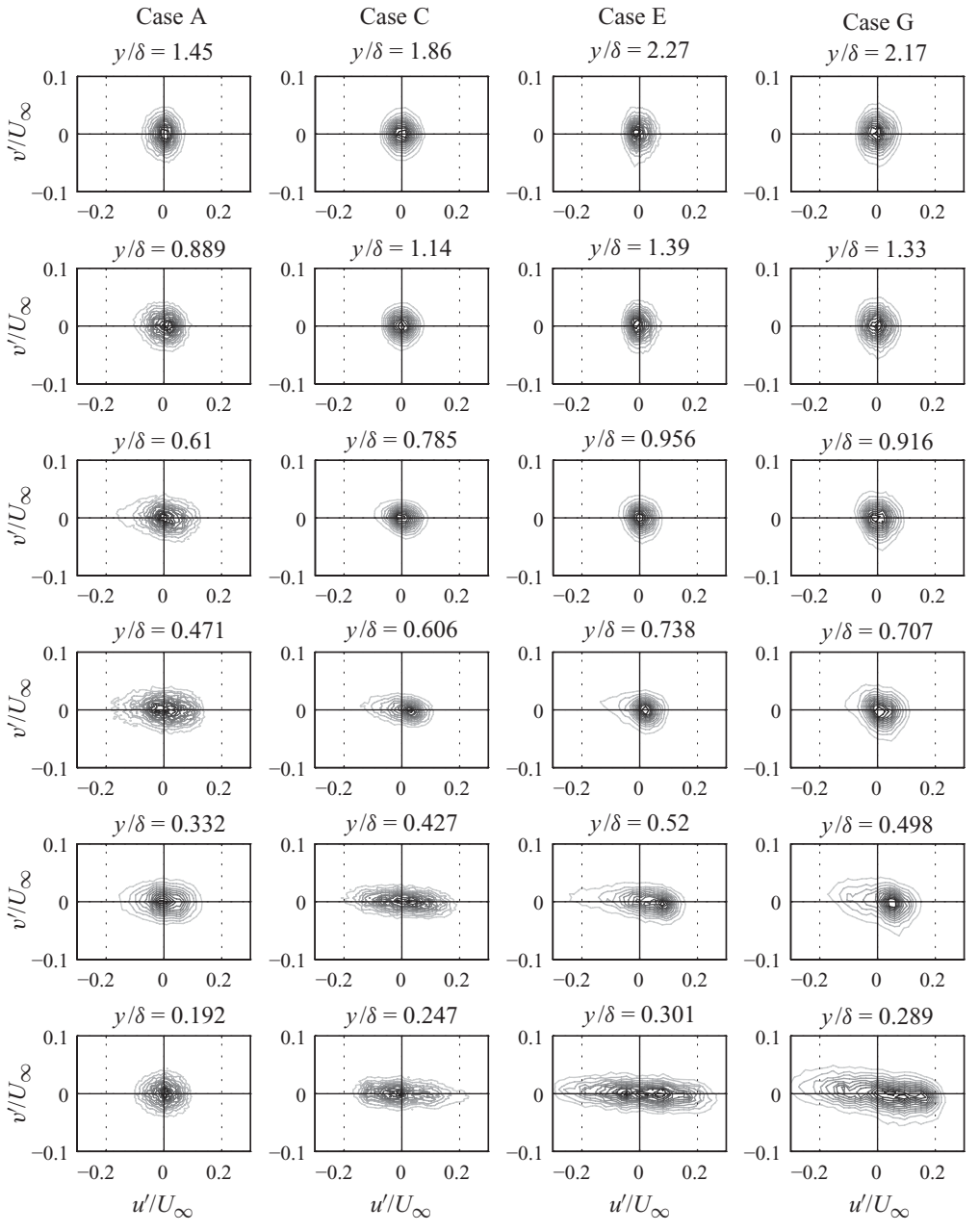

FIGURE 9. Joint PDFs for the fluctuating velocities of Cases A, C, E and G at notes positions from the wall.

stretched along the X-axis only for all cases as one moves closer to the wall. This stretching becomes increasingly pronounced in subsequent cases. Additionally, there is a clockwise rotation of the elliptical shape of the joint PDF into the Q2 and Q4 quadrants indicating increasingly turbulent-like behaviour. Positive disturbances are restricted to the inner half of the boundary layer. In the outer half of the boundary layer ($0.5 < y/\delta < 1$) for Cases C–G the peak of the joint PDFs is shifted to the

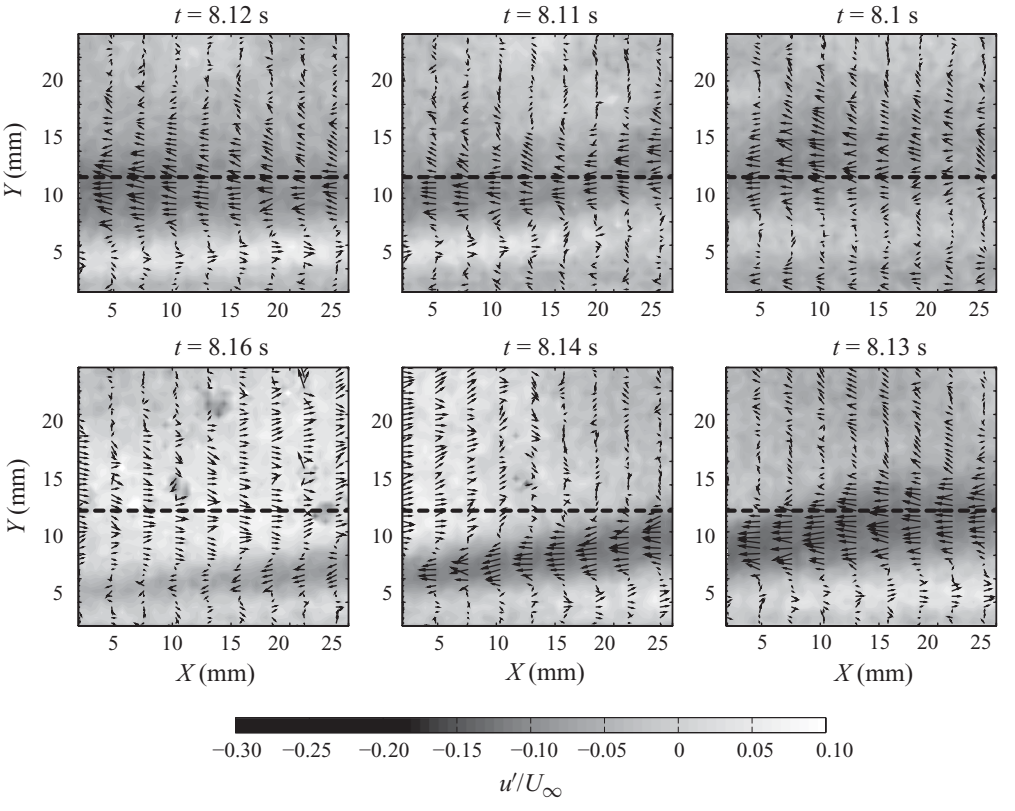

FIGURE 10. Negative event for Case C indicated by dark-coloured contours.

right and a long tail that extends into the second quadrant is visible. This suggests that large-amplitude negative streamwise fluctuations skew the data in this region.

Figures 10–12 show vector maps of the instantaneous flow structure found at the extreme ends of the joint PDFs shown in figure 9 where the hole size, H, is at its largest. Figure 10 shows a negative streak from Case C with a significant lift-up angle. The streak extends well beyond the mean boundary-layer thickness. Figures 11 and 12 correspond to negative and positive streamwise positions at the extreme ends of the joint PDFs for Case G and therefore include significant wall-normal perturbations. Additional events are also observed in the instantaneous vector maps at various wall-normal positions. The sequences show strong regions of both positive and negative perturbation indicating the direct interaction between these large-amplitude events. The positive perturbations show a clear sweeping behaviour while the negative perturbations show notably large amounts of ejection. The interaction between positive and negative perturbations at $t = 1.69$ s in figure 12 result in a sharp shear interface similar to those found in the simulations of Brandt & de Lange (2008). The spatial arrangement of patches of ejection in figure 11 at the mean boundary-layer edge above fast moving sweeping flow near the wall is similar to the 'eruption' event described by Jacobs & Durbin (2001). As discussed previously these two scenarios posit different sources and wall-normal locations for the inception of a turbulent spot. In order to investigate if these scenarios are playing a role in the

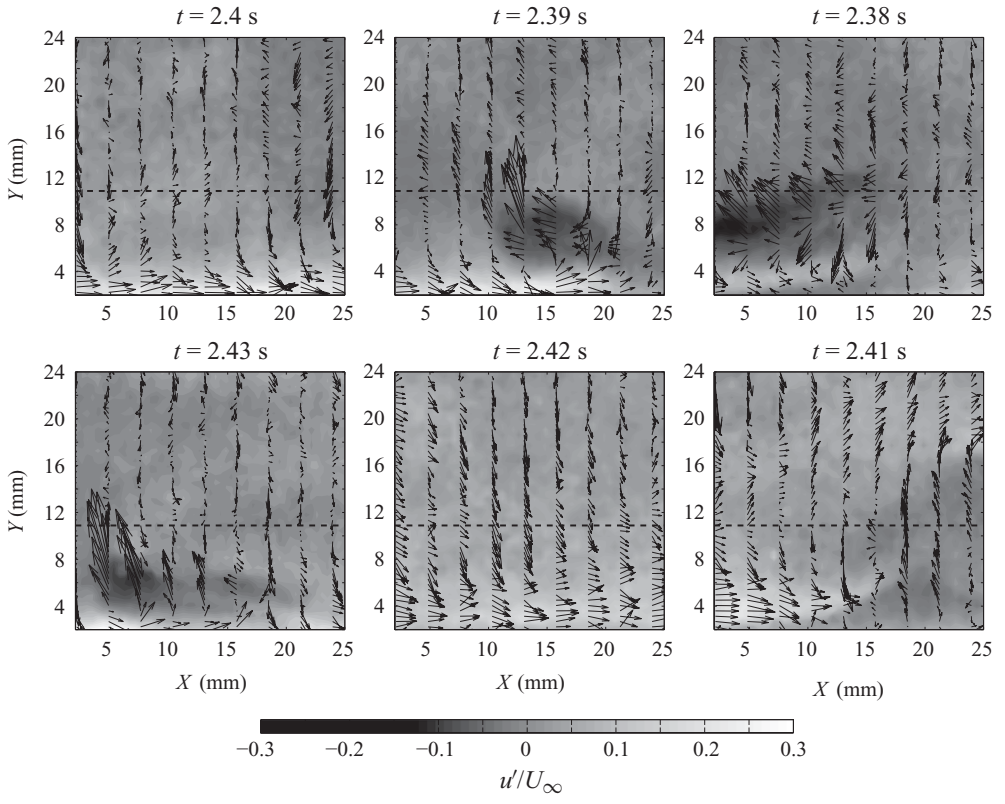

FIGURE 11. Strong negative event for Case G exhibiting strong ejection indicated by dark-coloured contours. A concurrent positive event is also observed close to the wall.

current data it is necessary to determine the point at which transition begins. To do this, it is useful to calculate the turbulence production level across all cases.

The production of TKE for a two-dimensional boundary layer with negligible pressure gradient can be simplified as (Schlichting 1979)

$$P_{TKE} = -\overline{u'v'}\frac{\mathrm{d}\overline{U}}{\mathrm{d}y}. \tag{3.1}$$

Figure 13 shows a contour plot of the production of TKE across the entire experimental domain. The X-axis labels are positioned at the local Reynolds number for each case while the contours represent non-dimensional production of TKE in terms of friction velocity:

$$P^*_{TKE} = \frac{-\overline{u'v'}}{u_\tau^2}\frac{\mathrm{d}U^+}{\mathrm{d}Y^+}. \tag{3.2}$$

It can be seen that P^*_{TKE} peaks away from the wall in the pre-transitional cases where production results from the streaky structures and then moves wallwards due the formation of turbulent spots in the transition region (Cases E–H). This is accompanied by a significant rise in the level of P^*_{TKE}. This is similar to the findings of Walsh *et al.* (2007) where conditionally sampled hot-wire data from the literature (Volino, S. & Pratt 2003) was analysed to identify regions of elevated volumetric entropy generation rate. Since the turbulence production term in (3.1) was used

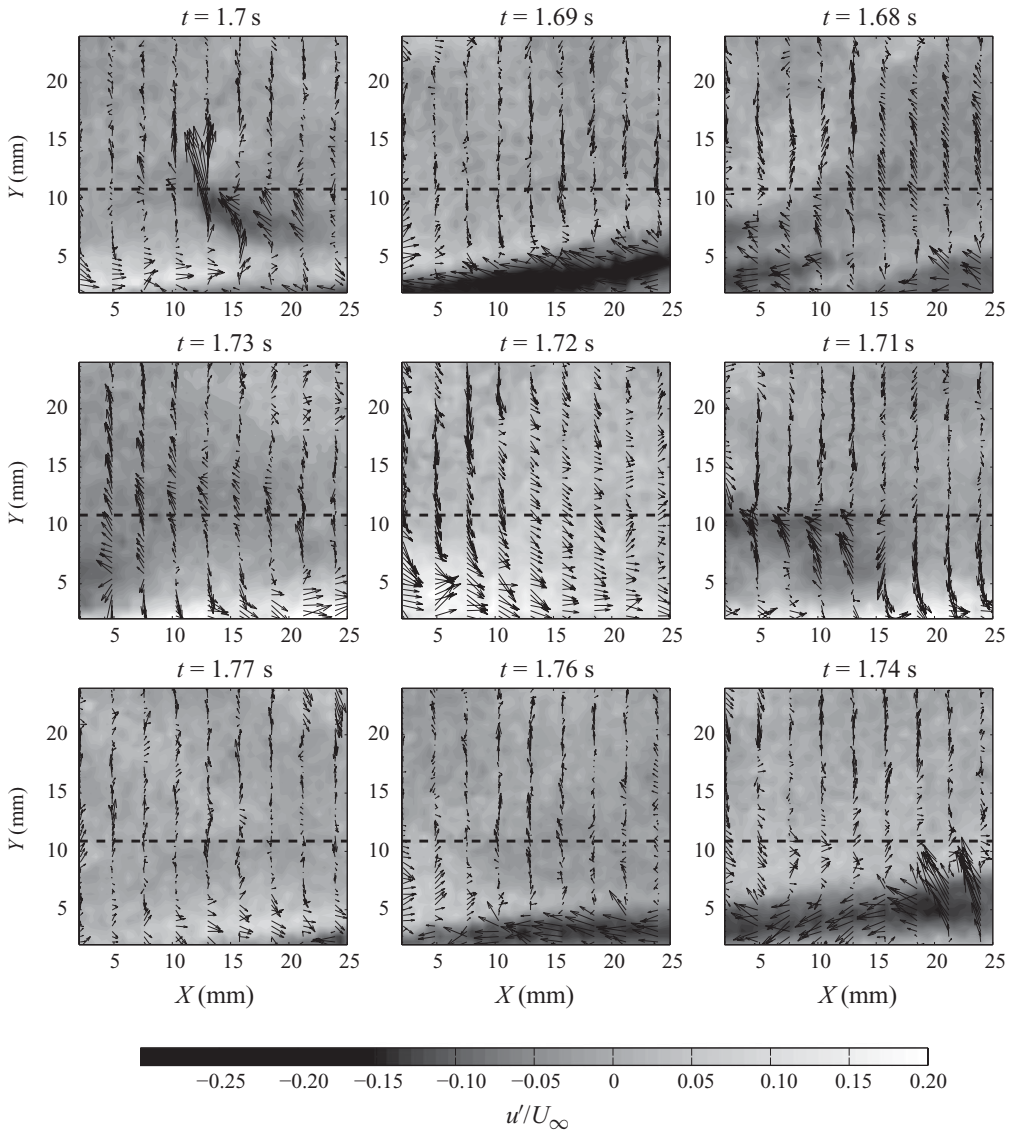

FIGURE 12. Strong positive event for Case G close to the wall indicated by light-coloured contours. Strong negative events are observed directly before and after the event.

to estimate the turbulence dissipation term (see Walsh, McEligot & Nolan 2007), parallels can be drawn with the current data. The study by Walsh *et al.* (2007) found a number of peaks in the time-averaged volumetric entropy generation rate in the early stages of the transition process. The conditional sampling technique applied to the data by Volino *et al.* (2003) allowed determination of the viscous and Reynolds shear stress contributions to the entropy generation separately, eliminating these peaks. It was concluded by that the conditional sampling technique filtered out artificially large Reynolds stresses induced by time averaging of a highly intermittent time series containing turbulent spots, which travel at a higher local velocity than the 'non-turbulent' flow. The quadrant analysis employed in the current study provides

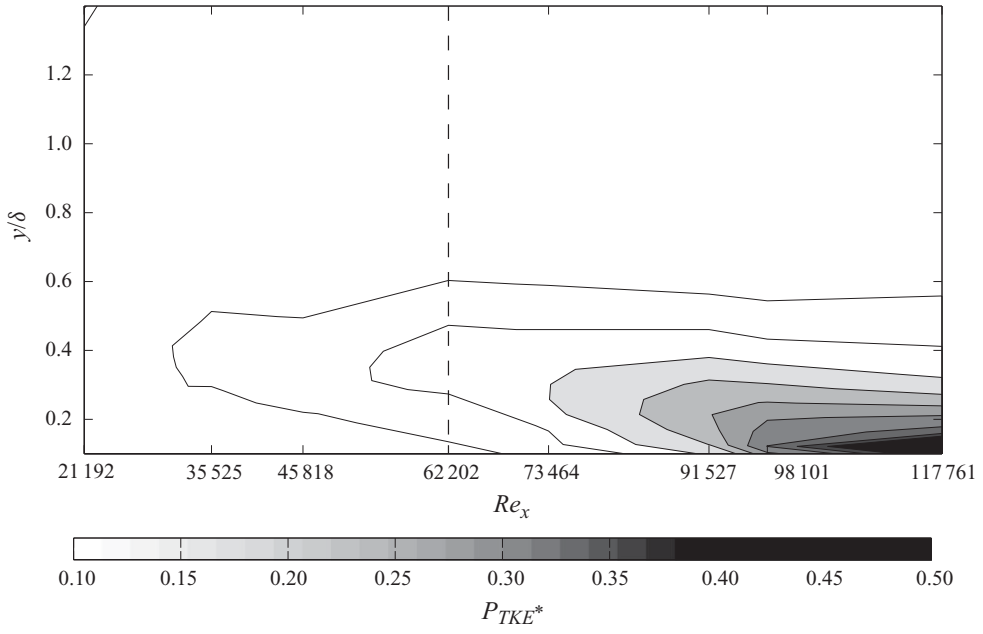

FIGURE 13. Production of kinetic energy (defined in (3.2)) for the experimental domain, X-axis labels correspond to each test case. Dashed line indicates point of transition onset. Contour lines increment from 0 to 0.5 in 0.055 steps.

the opportunity to examine the effects of instantaneous fluctuations on the time-averaged statistics. This is seen, particularly, clearly in figure 9 where long tails in the distributions of the data are found.

Figure 14 shows contours of P^*_{TKE} for the decomposed $u'v'$ quadrants according to

$$P_{TKE}i = -\overline{u'v'}_i \frac{\mathrm{d}\overline{U}}{\mathrm{d}y}, \tag{3.3}$$

where

$$\sum_{i=1}^{4} P_{TKE}i = P_{TKE}. \tag{3.4}$$

Quadrants 2 and 4 are the main contributors to P^*_{TKE} with quadrants 1 and 3 providing almost identical small contributions (opposite in sign to quadrants 2 and 4). In the pre-transitional region the peak production occurs away from the wall for all quadrants at $y/\delta \approx 0.3$ moving wallwards with increasing Reynolds number. Quadrant 4 contours are compressed together close to the wall with increased Reynolds number compared to the Q2 quadrant. The Q2 quadrant remains more evenly distributed across the boundary-layer thickness in the transition region. Otherwise the Q2 and Q4 contributions to turbulence production are similar in shape and magnitude. This growth in turbulence production away from the wall indicates that breakdown to turbulence occurs away from the wall. It does not appear however at the boundary-layer edge. The coupled large-eddy and direct simulations of Nagarajan, Lele & Ferziger (2007) show, for a sharp leading edge, that the initial precursor to a turbulent spot occurs in the outer half of the boundary layer with the fluid close to the wall being unaffected by spot formation. They note that the lower part of the boundary layer (and hence the skin friction) is affected only after the instability grows and

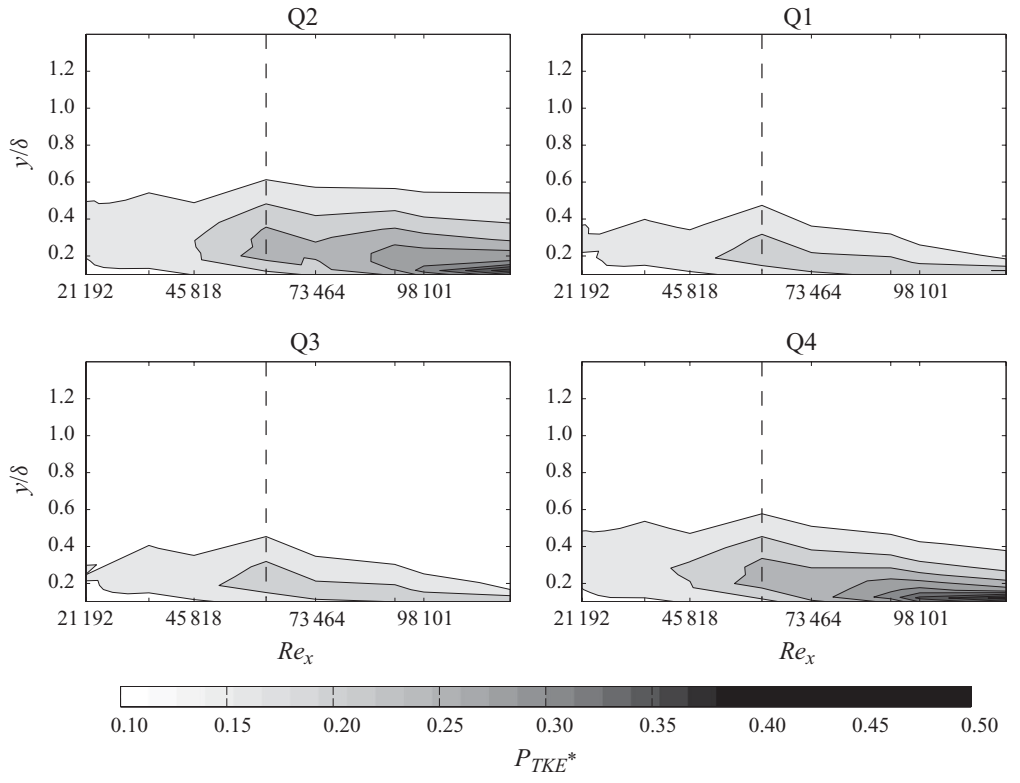

FIGURE 14. TKE production per quadrant as in figure 13.

further breakdown leads to spot formation (Nagarajan *et al.* 2007). This suggests that vertical transport of free-stream disturbances downwards into the boundary layer rather than production in this region is a likely candidate for the initiation of a turbulent spot. The present data however shows that the main contribution to turbulence production occur within the inner half of the boundary layer. Examination of the vector maps shown above show that the flow is dominated by lifted negative streaks and positive streaks confined to the wall. They are found to interact with each other within the inner half of the boundary layer.

Figures 15–18 show contour maps presenting the results of the quadrant hole analysis. Typically such data is plotted at selected wall-normal positions in the form of a cartesian plot (Willmarth & Lu 1972). This, however, can mask important trends in the stress and duration fractions. Shown in each figure are four contour maps, one for each quadrant and labelled accordingly. The *X*-axis represents the hole threshold level ($H(u'_{rms}v'_{rms})$) while the *Y*-axis represents the wall-normal position normalized by the local boundary-layer thickness. The plot consists of two superimposed contour plots; a continuous grey scale contour plot and discrete isolines. The continuous grey scale contours show the stress fraction or contribution to the total Reynolds shear stress. The black isolines show the duration fraction and are superimposed over the stress fraction contours. Grey scale contours bunched tightly to the left suggest that only small-scale fluctuations contribute most to the Reynolds shear stress while contours that extend for several multiples of the threshold show that large-amplitude fluctuations are present at this particular wall-normal location and contribute to the total Reynolds shear stress accordingly. The duration fraction isolines indicate

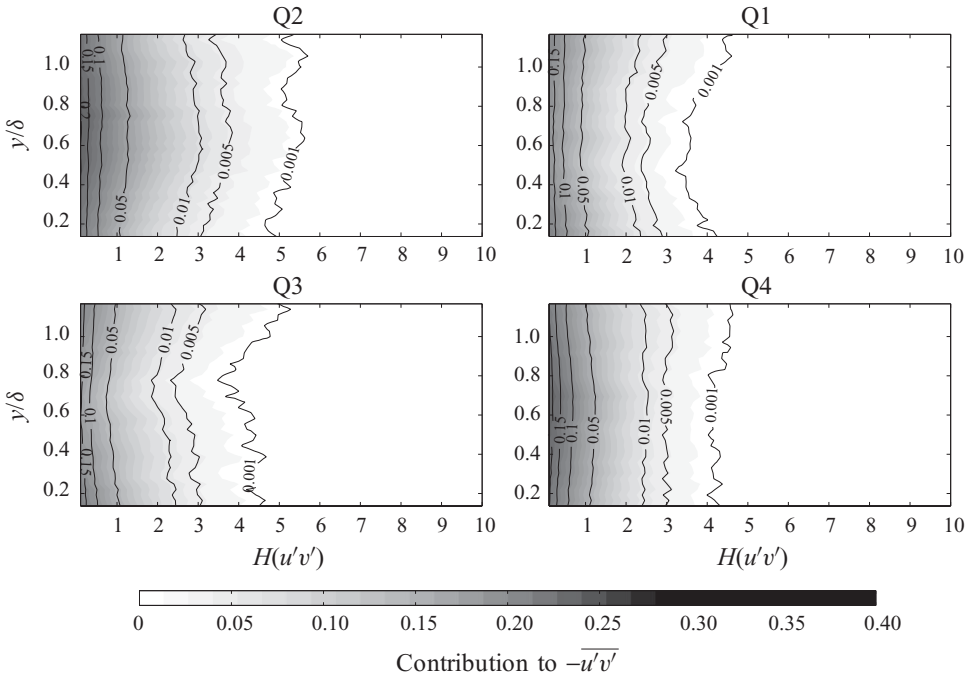

FIGURE 15. Grey scale contours of stress fraction for Case A for each quadrant normal to the wall with isolines of duration fraction superimposed.

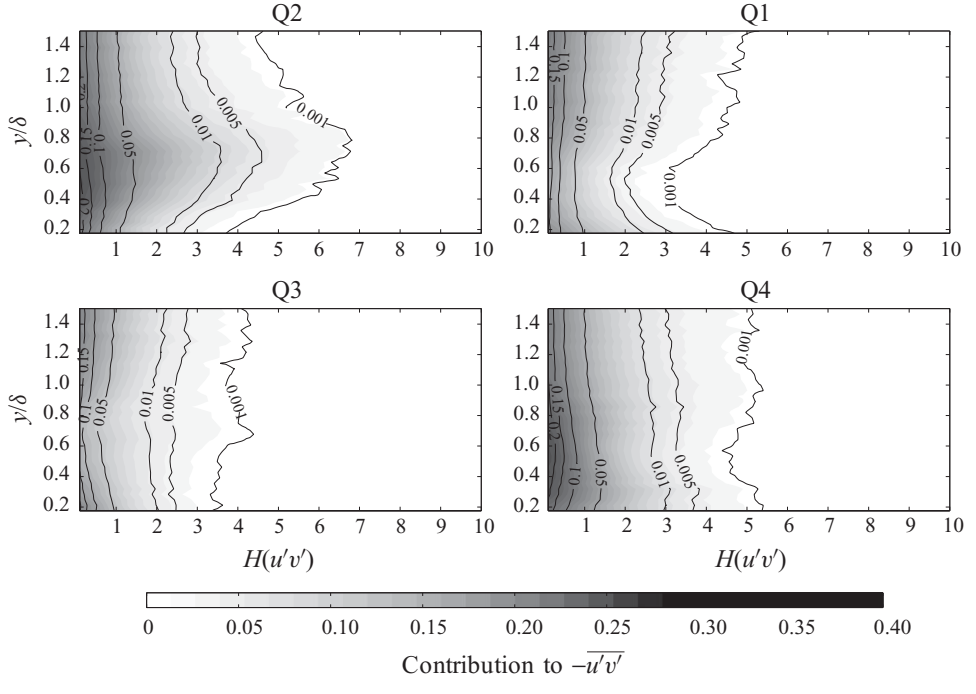

FIGURE 16. Contours of stress fraction for Case C for each quadrant with isolines of duration fraction superimposed.

the proportion of time which the measurements contribute to the indicated stress fraction. Therefore one can use these plots to determine the percentage contribution to the Reynolds shear stress by the associated percentage of time at any wall-normal position and the relationship to all other positions.

Since the pre-transitional streaks are generally confined to the streamwise perturbation velocity, it is proposed that any significantly large shear stress is therefore likely to be due to the production of TKE due to instabilities of the streaks, the influences of the streaks on the surrounding undisturbed flow, interactions with other streaks and free-stream disturbances. Stable streaks are precluded by the shape of the hole region for $H \neq 0$ which will filter one-dimensional perturbations.

For Case A (figure 15), the distributions for the four quadrants are quite similar. There is a slight bias towards Q2 events towards the boundary-layer edge at $y/\delta \approx 0.6$ compared to Q3 indicating that large-amplitude negative streamwise perturbations are preferentially lifted. The Q4 distribution is effectively flat across the boundary layer. This symmetry suggests that contributions to the Reynolds shear stress profile in this pre-transitional case are of small amplitude and are distributed relatively evenly between the quadrants. By Case C (figure 16), the growth in Q2 is notable with the formation of a clear peak while there is a corresponding deficit in Q1 at $y/\delta = 0.5$. The location of the Q2 peak moves further away from the wall with increasing threshold level as the contribution to Reynolds shear stress varies from 25 % to 2 %. The duration fraction varies from 5 % to 0.1 % in this region indicating that 25 % of the contribution to the Reynolds shear stress results from just 5 % of the time. There is also a trend of increasing in Q4 events towards the wall with 18 % of $-\overline{u'v'}$ being generated by 5 % of the flow time ($y/\delta = 0.2$).

Moving into the transition region with Cases E and G (figures 17 and 18), the trend found with the pre-transitional cases has increased significantly. The extent of Q2 fluctuations now surpasses the base threshold ($H = 1$) by a factor of 9 for Case E and 12 times for Case G (contributing to 13 % of $-\overline{u'v'}$ for just 1 % of the time). Quadrant 4 becomes damped at $y/\delta = 0.5$ and grows increasingly large near the wall, approaching stress fractions similar to those for quadrant 2. There is also a new Q3 peak visible in Case G.

The quadrant analysis presented here shows an almost simultaneous increase in wall sweeps at the wall with an increase in ejections in the outer region of the boundary layer. Distinct turbulent spot signatures are found to occur after Case D (figure 5), and this is accompanied by the increase in large-amplitude Q4 sweep events close to the wall as well as a large increase in the amplitude of Q2 ejection events. As seen in figures 12 and 11, these events can occur at the same time.

Several researchers have presented such data for turbulent flows in which they have commented on the relationship between the stress and duration fractions in terms of a percentage contribution to the Reynolds shear resulting from a percentage of the time (the duration fraction) for some arbitrary value as also presented above. The relationship between the stress and duration fractions can, however, be represented with a power law of the form $y = a(x^b + c)$. Good agreement is found, as seen in figure 19, for data within a hole size of $1 \leqslant H \leqslant 10$ (H is not shown in figure 19; corresponding data points represents discrete values of H for each quadrant. Data for $H > 1$ are represented by open circles). This approach therefore allows the determination of the entire contribution to the Reynolds shear stress to be determined. While stating arbitrary values can be highly descriptive, particularly when describing the influences of turbulent bursts, it provides little information for model validation and development.

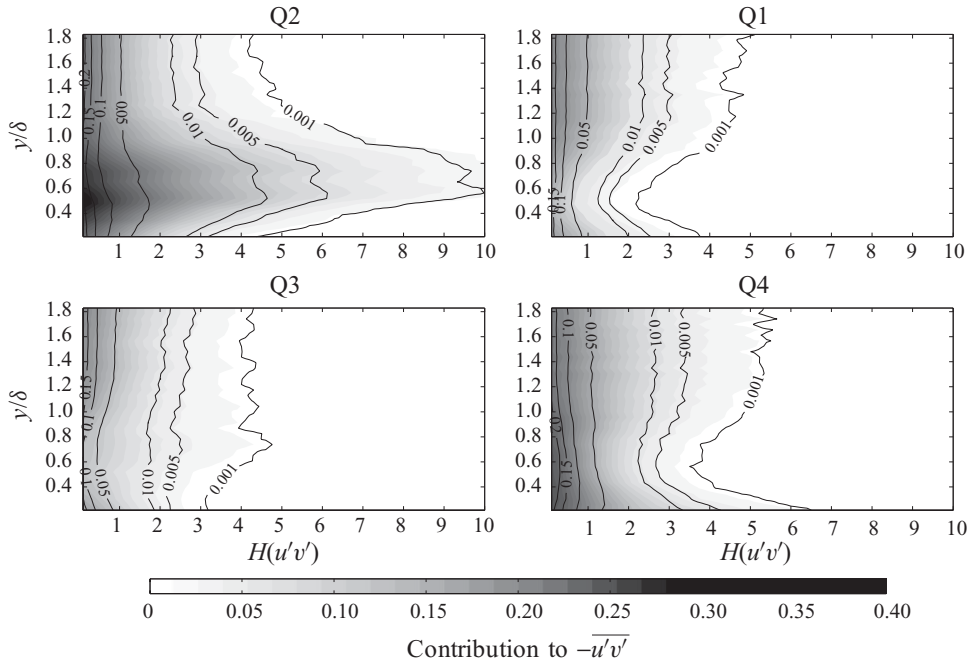

FIGURE 17. Contours of stress fraction for Case E for each quadrant with isolines of duration fraction superimposed.

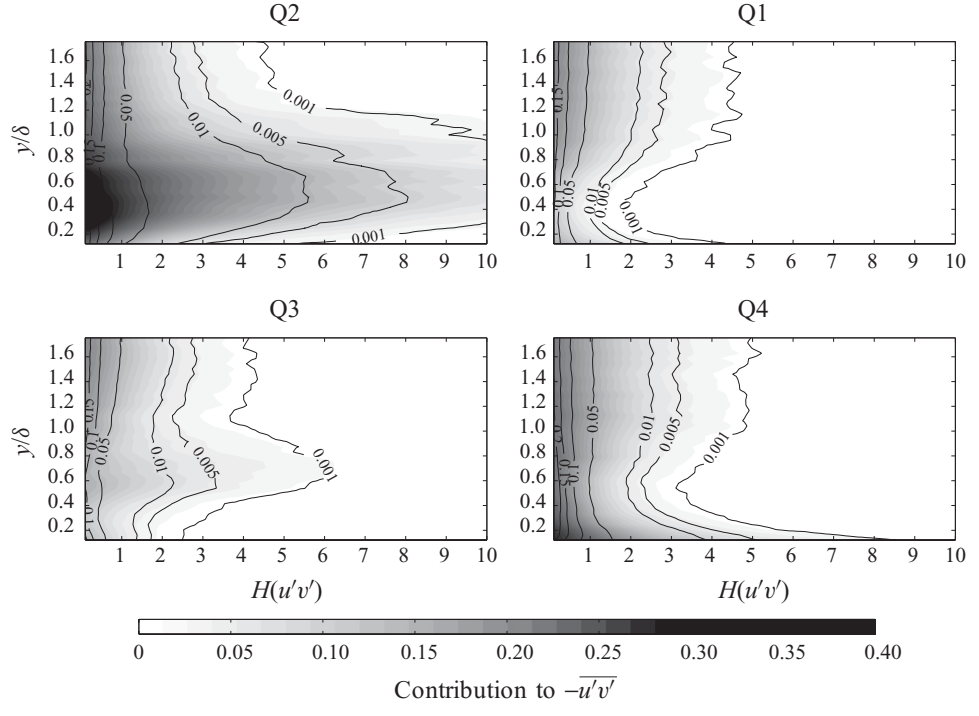

FIGURE 18. Contours of stress fraction for Case G for each quadrant with isolines of duration fraction superimposed.

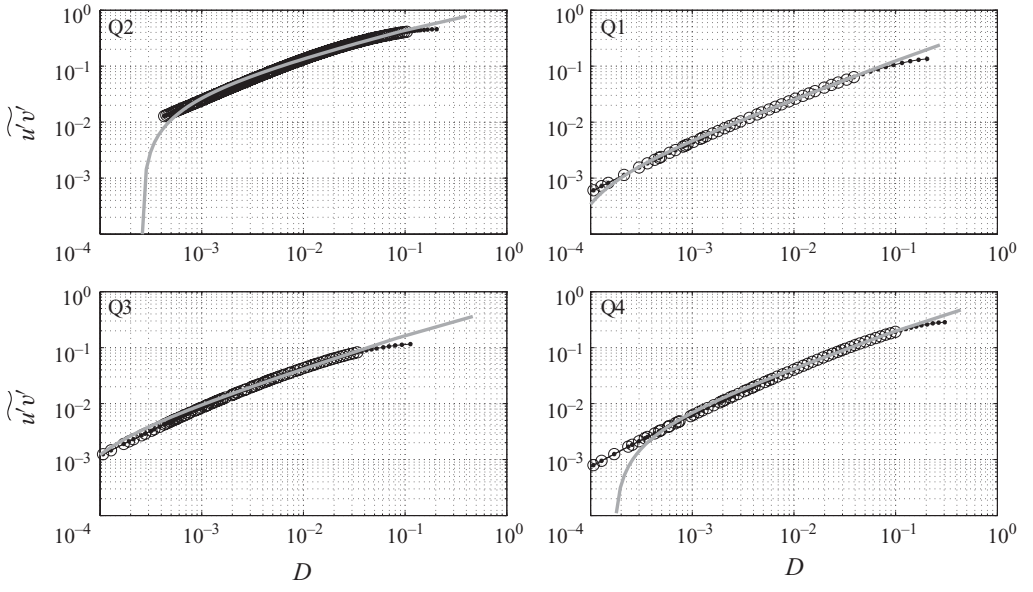

FIGURE 19. Power-law fit of stress and duration fraction (D) data for Case E at 5.4 mm from the wall, open circles show fitted data for $1 \leqslant H \leqslant 10$, closed circles show the entire data series for $0 \leqslant H \leqslant 10$.

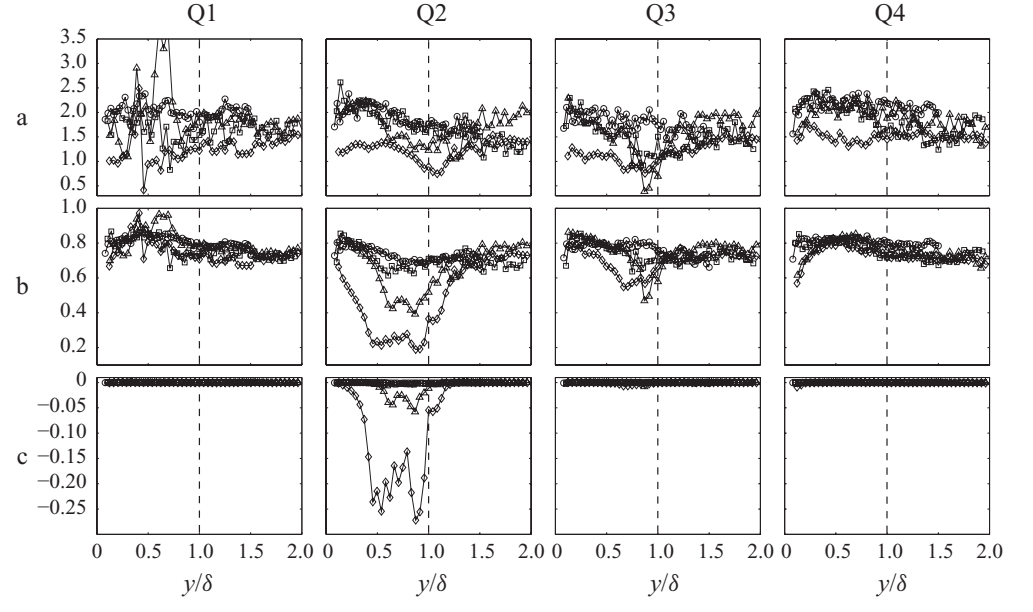

FIGURE 20. Power-law coefficients a, b and c for Cases A, C, E and G denoted by ○, □, △, ◇, respectively

The resulting curvefits are similar for all quadrants except quadrant 2 which is higher indicating a greater contribution to the Reynolds shear stress results from a similar duration fraction. Figure 20 shows the distribution of the power-law coefficients a, b and c obtained for Cases A, C, E and G for each quadrant. The additive

coefficient, c, remains relatively similar for all cases remaining effectively zero for quadrants 1, 3 and 4. The multiplicative coefficient, a, remains between 1 and 2.5 for all quadrants decreasing with increased Reynolds number for all quadrants. The exponential coefficient, b, exhibits a somewhat uniform value of 0.8 in the pre-transitional cases across the boundary layer. For quadrant 2 this drops rapidly towards 0.2 for Case G in the outer 50 % of the boundary layer. This change in exponential coefficient is accompanied by a similar drop in the additive coefficient, c, for Cases E and G.

The simulations of Zaki & Durbin (2005) and Nagarajan *et al.* (2007) show large ejections of fluid close to the mean boundary-layer edge prior to breakdown. This corresponds to the upwelling of lifted negative streaks and is found to be important in the breakdown process via a complex three-dimensional instability. Once this breakdown occurs, the disturbances are transported towards the wall resulting in a turbulent spot. This scenario results in the formation of large vortical disturbances at the boundary-layer edge. Figures 21–24 show vorticity ratios (defined in (2.7)) for each quadrant in a similar manner to the stress fractions in figures 15–18. Contours represent the mean unidirectional spanwise component of vorticity for the data in each quadrant that satisfies the hole region threshold. The vorticity ratio as previously stated is not a fraction like the stress fraction but a measure of the mean vorticity associated with the remaining data beyond the specified threshold divided by the total positive or negative vorticity. Figures 21 and 23 represent the positive vorticity (contour clockwise rotation when the flow is from left to right) and figures 22 and 24 the negative (clockwise) vorticity for Cases E and G, respectively.

There is little variation in the vorticity ratio for positive vorticity in Case E (figure 21), across all four quadrants. There is however a narrow region of elevated positive vorticity at $y/\delta \approx 0.2$ beyond a hole size of 3 in the fourth quadrant. The negative vorticity data is much different. Quadrants 2 and 3, which correspond to negative u' disturbances and therefore fluctuations related to negative streaks, such as turbulent spots, show a large region of elevated negative spanwise vorticity (dark contour) in the outer half of the boundary layer. This extends beyond the mean boundary-layer thickness for both quadrants. There is a corresponding reduction in negative vorticity (light contour) in quadrants 1 and 4 within the boundary layer. Similar behaviour is found for Case G, figures 23 and 24. This indicates that the lifted negative streaks are associated with elevated vorticity at and beyond the boundary-layer edge while positive streaks close to the wall tend to show a preference for positive vorticity close to the wall. As previously noted, the shape of the hole region will eliminate one-dimensional disturbances such as stable streamwise streaks. Consequently, this should also filter out vorticity due to the local shear within these structures which results from one-dimensional perturbations. Therefore the elevated regions of vorticity, particularly at large threshold values, are likely to be due to vortical structures resulting from instabilities.

While the production of TKE is concentrated near the wall in Cases E and G there is a significant level of negative vorticity in the outer region of the boundary layer directly above this region. This, and the large-amplitude quadrant 2 Reynolds shear stress in this region, indicates that there may be a transport mechanism where negative streaks lifted to the boundary-layer edge are involved the increase in turbulence production inside the boundary layer.

Close to the wall there is a region of positive vorticity in quadrant 4. The interaction of fast moving positive streaks close to the wall and slow moving lifted negative streaks will results in regions of high shear as the streaks collide either longitudinally

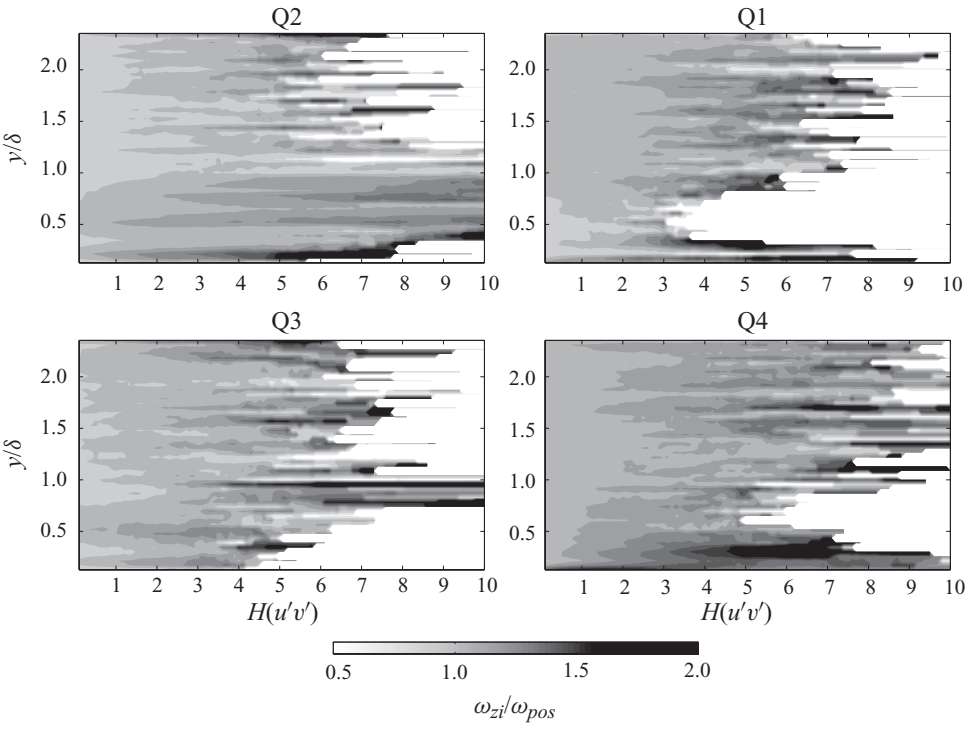

FIGURE 21. Grey scale contours of positive vorticity ratio for Case E.

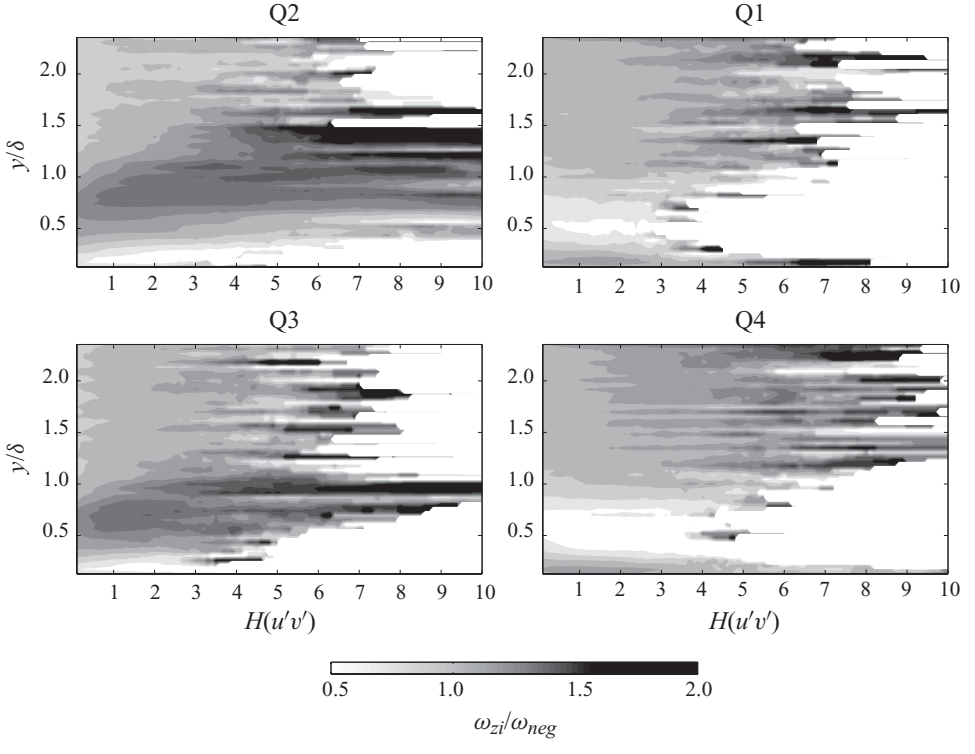

FIGURE 22. Contours of negative vorticity ratio for Case E.

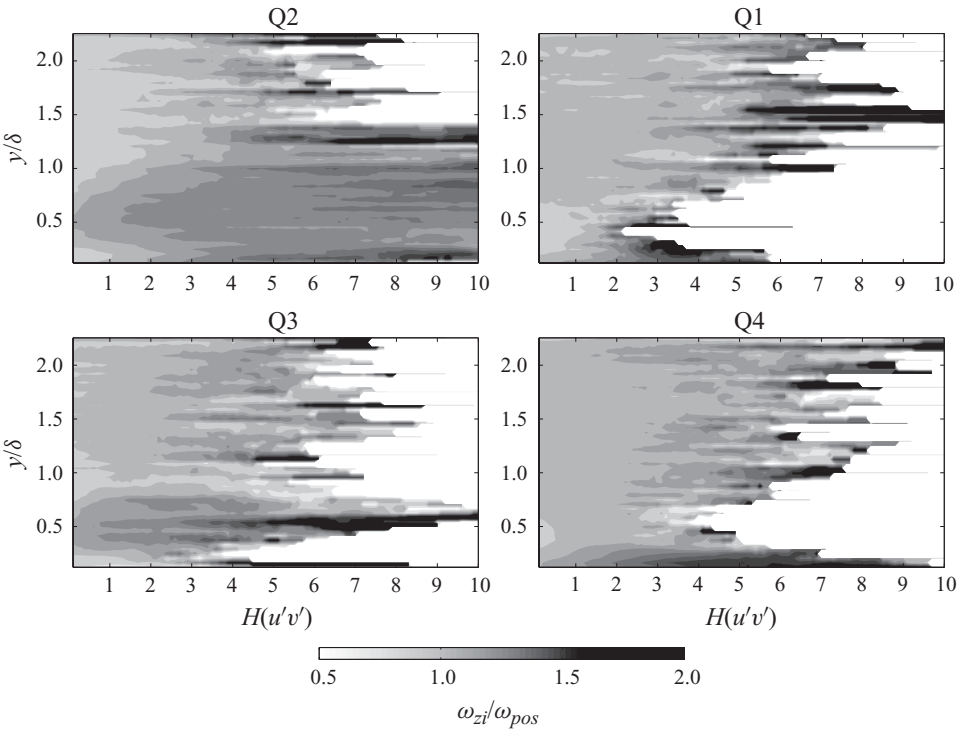

FIGURE 23. Contours of positive vorticity ratio for Case G.

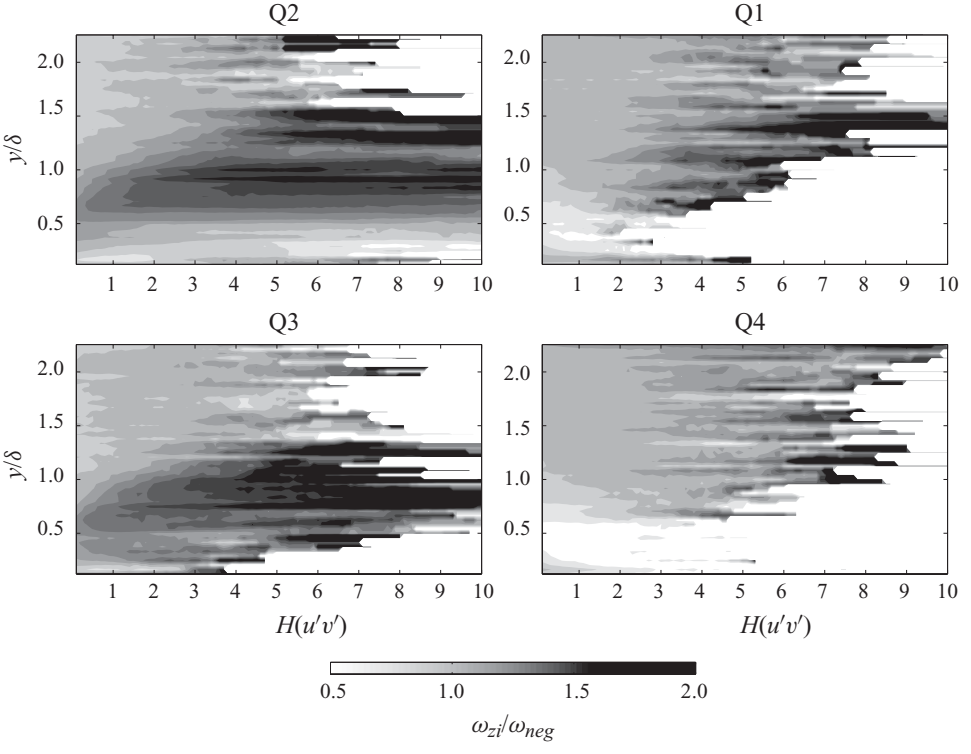

FIGURE 24. Contours of negative vorticity ratio for Case G.

and laterally as simulated by Brandt & de Lange (2008). Vortical structures were observed to form around symmetrical collisions between upstream positive streaks and downstream negative streaks. Since positive streaks remain close to the wall and negative streaks are lifted upwards, collisions between the lifted slower fluid and faster fluid close to the wall would be expected to result in regions of positive vorticity close to the wall as found in figures 21 and 23.

4. Conclusions

This paper presents several interesting observations on the route to bypass transition. These further confirm the important role that streamwise streaky structures, in the presence of free-stream disturbances, play in the breakdown to turbulence. Similarities with recent direct numerical simulations are found, such as the regions of strong ejection at the boundary-layer edge, which are similar to the spot precursor instabilities of Zaki & Durbin (2005) and Nagarajan *et al.* (2007), and the sharply defined shear interface found between colliding streaks (Brandt & de Lange 2008). The sharp rise in heat flux found in the hot-film turbulent spot signatures appears to result from this shear interface. The breakdown of this interface would then account for the fluctuations found at the peak of the signature with increased spot maturity, as illustrated by Anthony *et al.* (2005), with the remainder of the fast moving streak resulting in the so called 'calmed' region.

The initial growth in P_{TKE} is observed to occur away from the wall ($y/\delta \approx 0.3$) in the pre-transitional region. The point of transition is defined by the measurement of a turbulent spot by the hot-film sensor. The P_{TKE} peak moves steadily towards the wall with increased Reynolds number. This initial growth in P_{TKE} still occurs within the inner half of the boundary layer and not at the boundary-layer edge. This favours the streak interaction scenario for spot formation rather than breakdown at the boundary-layer edge. However the possibility of small-scale free-stream disturbances being transported into the boundary layer is not ruled out as the PIV method is generally limited to the larger scales due to spatial filtering by the cross-correlation method.

The growth in Q2 events at the boundary-layer edge with the accompanying increase in vorticity ratio for quadrants 2 and 3 indicates the presence of large-scale disturbances in this region. These disturbances appear to result primarily from lifted negative streaks and interaction with the high-velocity fluid around them. These disturbances should not appear in the time-averaged turbulence production data, since the local shear here results from individual streaks. Since the quadrant hole method filters vorticity resulting solely from the streamwise velocity gradient, the resulting disturbances have a significant vertical component. This is observed particularly in figures 11 and 12. The duration of these events is shown to be short in the vector maps and by the small values of the duration fractions at these points. Since these short but violent ejections occur within the boundary layer in regions of streak interaction with magnitudes similar to local negative streaks, it may be assumed that they are unstable negative streaks. Both type of streak instability, varicose and sinuous, as observed by Mans *et al.* (2005), would appear similar in the $X-Y$ two-dimensional measurement plane used in the current work as only the spanwise extremities of the unstable streaks enter the laser sheet.

The relationship between the duration and the stress fractions is shown to be well represented by a power law, the Q2 exponent of which shifts significantly for much of the boundary-layer thickness after transition begins. This indicates that a

greater proportion of the shear stress is being generated by shorter periods of time as Reynolds number increases, and therefore these fluctuations are responsible for much of the turbulence production. The power-law data makes the entire contribution to the Reynolds shear stress across the boundary layer available. This should prove useful to the turbulence modelling community as the data provides the range of frequency and strength of disturbances in the transition region which will allow for greater validation than can be obtained from time-averaged data alone.

REFERENCES

Adrian, R. J., Meinhart, C. D. & Tomkins, C. D. 2000 Vortex organization in the outer region of the turbulent boundary layer. *J. Fluid Mech.* **422** (1), 1–54.

Alfredsson, P. H. & Johansson, A. V. 1984 On the detection of turbulence-generating events. *J. Fluid Mech. Digit. Arch.* **139** (1), 325–345.

Anthony, R. J., Jones, T. V. & LaGraff, J. E. 2005 High frequency surface heat flux imaging of bypass transition. *J. Turbomach.* **127**, 241–250.

Brandt, L. & de Lange, H. C. 2008 Streak interactions and breakdown in boundary layer flows. *Phys. Fluids* **20** (2), 024107.

Brandt, L., Schlatter, P. & Henningson, D. S. 2004 Transition in boundary layers subject to free-stream turbulence. *J. Fluid Mech.* **517** (1), 167–198.

Cantwell, B., Coles, D. & Dimotakis, P. 1978 Structure and entrainment in the plane of symmetry of a turbulent spot. *J. Fluid Mech. Digit. Arch.* **87** (04), 641–672.

Chong, T. P. & Zhong, S. 2005 On the three-dimensional structure of turbulent spots. *J. Turbomach.* **127** (3), 545–551.

Durbin, P. & Wu, X. 2007 Transition beneath vortical disturbances. *Annu. Rev. Fluid Mech.* **39** (1), 107–128.

Fransson, J. H. M., Talamelli, A., Brandt, L. & Cossu, C. 2006 Delaying transition to turbulence by a passive mechanism. *Phys. Rev. Lett.* **96** (6), 064501.

Hernon, D., Walsh, E. J. & McEligot, D. M. 2007 Experimental investigation into the routes to bypass transition and the shear-sheltering phenomenon. *J. Fluid Mech.* **591** (1), 461–479.

Jacobs, R. G. & Durbin, P. A. 2001 Simulations of bypass transition. *J. Fluid Mech.* **428** (1), 185–212.

Klebanoff, P. S. 1971 Effect of free-stream turbulence on the laminar boundary layer. *Bull. Am. Phys. Soc.* **10**, 1323.

Lu, S. S. & Willmarth, W. W. 1973 Measurements of the structure of the Reynolds stress in a turbulent boundary layer. *J. Fluid Mech. Digit. Arch.* **60** (03), 481–511.

Mans, J., Kadijk, E., Lange, H. & Steenhoven, A. 2005 Breakdown in a boundary layer exposed to free-stream turbulence. *Exp. Fluids* **39** (6), 1071–1083.

Nagarajan, S., Lele, S. K. & Ferziger, J. H. 2007 Leading-edge effects in bypass transition. *J. Fluid Mech.* **572** (1), 471–504.

Roach, P. E. 1987 The generation of nearly isotropic turbulence by means of grids. *Intl J. Heat Fluid Flow* **8** (2), 82–92.

Sabatino, D. & Smith, C. 2002 Simultaneous velocity-surface heat transfer behavior of turbulent spots. *Exp. Fluids* **33** (1), 13–21.

Schlatter, P., Brandt, L. & De Lange, H. C. 2007 The effect of free-stream turbulence on growth and breakdown of Tollmien–Schlichting waves. In *Advances in Turbulence XI: Proceedings of the Eleventh European Turbulence Conference, Porto, Portugal* (ed. J. M. L. M. Palma & A. Silva Lopes), pp. 179–181. Springer.

Schlichting, H. 1979 *Boundary Layer Theory*. McGraw-Hill.

Schrder, A. & Kompenhans, J. 2004 Investigation of a turbulent spot using multi-plane stereo particle image velocimetry. *Exp. Fluids* **36** (1), 82–90.

Volino, R. J., Schultz, M. P. & Pratt, C. M. 2003 Conditional sampling in a transitional boundary layer under high freestream turbulence conditions. *J. Fluids Engng* **125** (1), 28–37.

Walsh, E. J., Hernon, D., Davies, M. R. D. & McEligot, D. M. 2005 Preliminary measurements from a new plate facility for aerodynamic research. In *Sixth European Turbomachinery Conference: Fluid Dynamics and Thermodynamics*, Lille, France.

Walsh, E. J., McEligot, D. & Nolan, K. 2007 A method for the management and prediction of entropy generation rates in turbulent boundary layers. In *Seventh European Turbomachinery Conference, Athens, Greece.*

Walsh, E. J., Nolan, K. P., McEligot, D. M., Volino, R. J. & Bejan, A. 2007 Conditionally-sampled turbulent and nonturbulent measurements of entropy generation rate in the transition region of boundary layers. *J. Fluids Engng* **129** (5), 659–664.

Willmarth, W. W. & Lu, S. S. 1972 Structure of the Reynolds stress near the wall. *J. Fluid Mech. Digit. Arch.* **55** (01), 65–92.

Yaras, M. I. 2007 An experimental study of artificially-generated turbulent spots under strong favorable pressure gradients and freestream turbulence. *J. Fluids Engng* **129** (5), 563–572.

Zaki, T. & Durbin, P. A. 2005 Mode interaction and the bypass route to transition. *J. Fluid Mech.* **531**, 85–111.

Zhu, W., van Hout, R. & Katz, J. 2007 PIV Measurements in the atmospheric boundary layer within and above a mature corn canopy. Part II. Quadranthole analysis. *J. Atmos. Sci.* **64**, 2805–2824.